Micron-sized liquid nitrogen-cooled indium antimonide photovoltaic cell for near-field thermophotovoltaics

Rodolphe Vaillon, Jean-Philippe Perez, Christophe Lucchesi, Dilek Cakiroglu, Pierre-Olivier Chapuis, Thierry Taliercio, Eric Tournié

Research Article | Vol. 27, No. 4 | 18 Feb 2019 | OPTICS EXPRESS A11
Optics EXPRESS

Micron-sized liquid nitrogen-cooled indium antimonide photovoltaic cell for near-field thermophotovoltaics

RODOLPHE VAILLON,[1,2,3,*] JEAN-PHILIPPE PÉREZ,[4] CHRISTOPHE LUCCHESI,[1] DILEK CAKIROGLU,[4] PIERRE-OLIVIER CHAPUIS,[1] THIERRY TALIERCIO,[4] AND ERIC TOURNIÉ[4]

[1] *Univ Lyon, CNRS, INSA-Lyon, Université Claude Bernard Lyon 1, CETHIL UMR5008, F-69621, Villeurbanne, France*
[2] *Radiative Energy Transfer Lab, Department of Mechanical Engineering, University of Utah, Salt Lake City, UT 84112, USA*
[3] *Instituto de Energía Solar, Universidad Politécnica de Madrid, 28040 Madrid, Spain*
[4] *IES, Univ. Montpellier, CNRS, F-34000 Montpellier, France*
[*] *rodolphe.vaillon@insa-lyon.fr*

Abstract: Simulations of near-field thermophotovoltaic devices predict promising performance, but experimental observations remain challenging. Having the lowest bandgap among III-V semiconductors, indium antimonide (InSb) is an attractive choice for the photovoltaic cell, provided it is cooled to a low temperature, typically around 77 K. Here, by taking into account fabrication and operating constraints, radiation transfer and low-injection charge transport simulations are made to find the optimum architecture for the photovoltaic cell. Appropriate optical and electrical properties of indium antimonide are used. In particular, impact of the Moss-Burstein effects on the interband absorption coefficient of n-type degenerate layers, and of parasitic sub-bandgap absorption by the free carriers and phonons are accounted for. Micron-sized cells are required to minimize the huge issue of the lateral series resistance losses. The proposed methodology is presumably relevant for making realistic designs of near-field thermophotovoltaic devices based on low-bandgap III-V semiconductors.

1. Introduction

Since the seminal idea of using evanescent modes of radiation to improve the performances of thermophotovoltaic (TPV) heat-to-electricity converters was proposed [1, 2], a quite large number of articles have been dealing with theoretical and numerical simulations of this concept of so-called near-field thermophotovoltaic (NF-TPV) devices [3–47]. In these articles, the predicted gains in electrical power output in the near field are indeed very promising. Even so, the first experimental observation has been made only very recently [48]. The long elapsed time before this successful experiment after the first published attempt [49] can be explained by the large numbers of challenges to overcome. The first one is building a nanoscale vacuum gap between a thermal emitter and a receiver, namely a photovoltaic (PV) cell, in such a way that evanescent waves contribute to increase thermal radiation between them. Nevertheless, the obstacle to measuring near-field thermal radiation was overcome multiple times over the last decade or so [45]. The second challenge is to build and maintain a large temperature difference between the thermal emitter (at T_e) and the photovoltaic cell (at T_c). As a matter of fact, energy conversion being ultimately limited by Carnot efficiency, a small temperature difference means poor expectations for good performances. In addition, in the recent experimental demonstration of a NF-TPV converter [48], even though the emitter and cell temperatures are 655 and 300 K, leading to a maximum (Carnot) efficiency of 54 %, the stated efficiency is only ~0.02 %. The

#347515 https://doi.org/10.1364/OE.27.000A11
Journal © 2019 Received 8 Oct 2018; revised 5 Dec 2018; accepted 5 Dec 2018; published 17 Jan 2019

main reason for that low efficiency is that the active area of the cell is substantially larger than the area of the emitter. More generally, a remaining challenge, somewhat overlooked so far, is to design, fabricate and operate a functional photovoltaic cell maximizing performances in the near field.

In this work, by taking into account fabrication constraints and physics of low-bandgap semiconductors, a comprehensive optimization of the photovoltaic cell in a NF-TPV converter is proposed, in the case where the semiconductor material is indium antimonide (InSb). In the first part, the framework for the analysis is presented in details. It specifies the architecture of the cell and conditions for it to be fabricated and operational. In particular, it is clearly established that assuming that the InSb cell will operate at 300 K [5, 11, 14, 18, 20, 24, 26, 32, 33, 44] is not practicable. Instead the cell must be cooled down, typically by liquid nitrogen at around 77 K. Because of this cooling constraint, the cell described in the present article is meant to be for a laboratory experiment, not for a practical device. Selection of the appropriate optical and electrical properties required for the radiation transfer and electrical transport is described. In particular, InSb being the III-V semiconductor which has the lowest bandgap (0.23 eV at 77 K), it becomes easily degenerate when negatively doped. As a consequence, the so-called Moss-Burstein effect [50, 51], i.e. the decrease in interband absorption [52], must be accounted for. In addition, absorption by the free carriers and the phonons must be included because it is has tremendous impacts on the efficiency of the converter, especially in the near field because of sub-bandgap phonon-polariton heat transfer [17]. Radiation transfer and electrical models, available elsewhere [10, 15, 27], are briefly reminded. In the following section, results are presented and discussed. Explanations of the resulting optimum layer thicknesses and doping concentrations are provided. It is shown that series resistance losses expected for thermophotovoltaic cells, in particular in the near field because of larger currents, can be mitigated by fabricating micron-sized cells.

2. Methodology

2.1. NF-TPV converter, operating limits and fabrication constraints of the PV cell

The near-field thermophotovoltaic converter under consideration is depicted in Fig. 1 (a). The active part of the photovoltaic cell is an indium antimonide (InSb) p-on-n junction, to be fabricated by means of solid source Molecular Beam Epitaxy (MBE). As a consequence, the p- and n-doped layers are to be grown on a typical n-doped InSb wafer with fixed thickness (t_{sub} = 500 μm) and doping concentration ($N_{d,sub}$ = 4 10^{17} cm^{-3}). A gold layer with fixed thickness (t_{brl} = 200 nm) at the back of the cell acts as a radiation reflector and contact layer for the electrons. There are also gold contacts at the front of the cell, assumed to be at the sides. The shape and size of the active zone of the cell not shadowed by the contacts have to be determined in order to minimize - or even avoid - series resistance losses. For this purpose annular front contacts are selected such that the active area of the cell is a disk with radius R_c. The emitter is brought close to the cell so as to fully cover the area limited by the front contacts. The vacuum gap thickness (d) separating the emitter from the cell is a variable parameter. When it is smaller than the characteristic wavelength of thermal radiation of the emitter (at temperature T_e), evanescent waves contribute to radiation transfer from the emitter to the cell [53], and thus increase cell's photocurrent, voltage and electrical power output [1, 2].

Operation at 300 K of an InSb cell in an NF-TPV converter was modeled in several articles [5,11,14,18,20,24,26,32,33,44], but is quite unlikely in practice. Since the intrinsic concentration of charges in InSb is huge at room temperature (n_i = 2 10^{16} cm^{-3}) [54] and contributes importantly to the dark current [55], conventional InSb p-n junction diodes are unable to deliver power substantially. Instead, they have to be cooled, typically at less than around 120 K [56, 57], or more complex architectures need to be designed to reach higher operating temperatures [58–61]. Another limitation to the operation of conventional p-n junctions at room temperature is the

requirement of highly doping the n-layer (typically 10^{19} cm^{-3} or more [20, 26, 34, 44]) to build a barrier to the diffusion of majority carriers through the junction. But high negative doping concentrations lead to transparency (see section 2.2) and in turn less photogeneration of charges in this layer, an effect which was mostly overlooked so far (despite a warning in [5]). Hence following our experience in previous research works [57, 61], it is chosen to design a diode that will operate properly at T_c = 77 K.

Given the current capabilities of near-field radiation measurement setups [45], a reasonable emitter temperature of 773 K (500 °C) is considered. Radiation transfer simulations in the near field indicate that among various options for the emitter material, graphite is that which maximizes absorption in the cell for photon energies above the bandgap of InSb at 77 K (0.23 eV). Spectral radiation flux absorbed by the p-n junction only or by the receiver (junction, substrate and gold reflector / contact layer) are shown on Fig.1 (b) with optimized parameters of the cell that will be provided in a subsequent section (case 2-1-1, section 3.2). By comparing fluxes in the cases where the emitter is graphite in the near field (vacuum gap thickness of 100 nm) and where the emitter is a blackbody in the far field, the near-field enhancement is clearly visible. It is also decided that InSb layers grown by MBE should not be thicker than 3 μm in total. Hence the design of the cell consists of making radiation and electrical simulations for finding the thickness (t_p and t_n, with $t_p + t_n = 3\mu$m) and doping concentration (N_a and N_d) of the p- and n-layers of the junction, and the radius (R_c) of the active part of the cell, that maximizes the electrical power output of the NF-TPV converter. To do so, proper electrical and optical properties must be used.

2.2. Electrical and optical properties

Even though in this work the temperature of the cell is set to be 77 K, for the sake of generality and further needs of properties at larger temperatures, dependence on temperature of indium antimonide electrical and optical properties is accounted for whenever possible. The selected main band parameters of InSb are given in Table 1.

Table 1. Main band parameters of indium antimonide.

fundamental bandgap $E_g[T]$ (eV)	$E_g[T=0] - \frac{\gamma T^2}{T+\beta}$, $E_g(T=0) = 0.235$ eV, $\gamma = 0.32\,10^{-3}$ eV K^{-1}, $\beta = 170$ K [62]
electron mass at rest m_0 (kg)	$0.9109\,10^{-30}$ [63]
effective masses, $m_e^*(m_0)$	0.0135 [62], data in [54] if the concentration of electrons is larger than 10^{14} cm^{-3}
$m_{hh}^*(m_0), m_{lh}^*(m_0)$	0.43, 0.015 [54]
$m_{dh}^*(m_0)$	$((m_{hh}^*)^{3/2} + (m_{lh}^*)^{3/2})^{2/3}$ [63]

The optical properties required for radiation transfer simulations are the real and imaginary parts of the complex permittivity (ε), as a function of angular frequency (ω in rad s^{-1}). Angular frequency and photon energy (E in eV) can be used interchangeably (with $E = h\omega/e$, $h = 1.054571596\,10^{-34}$ J s and $e = 1.60217733\,10^{-19}$ C). In the subsequent developments, the complex permittivity and complex refractive index may need to be converted from one to the other when necessary. The optical properties of graphite are taken from the database in [64]. For gold, a Drude model is used with parameters in [65].

The most important optical property is linked to interband absorption leading to photogeneration of electron-hole pairs in the p-n junction. The fundamental bandgap of InSb being low (E_g = 0.23

Optics EXPRESS

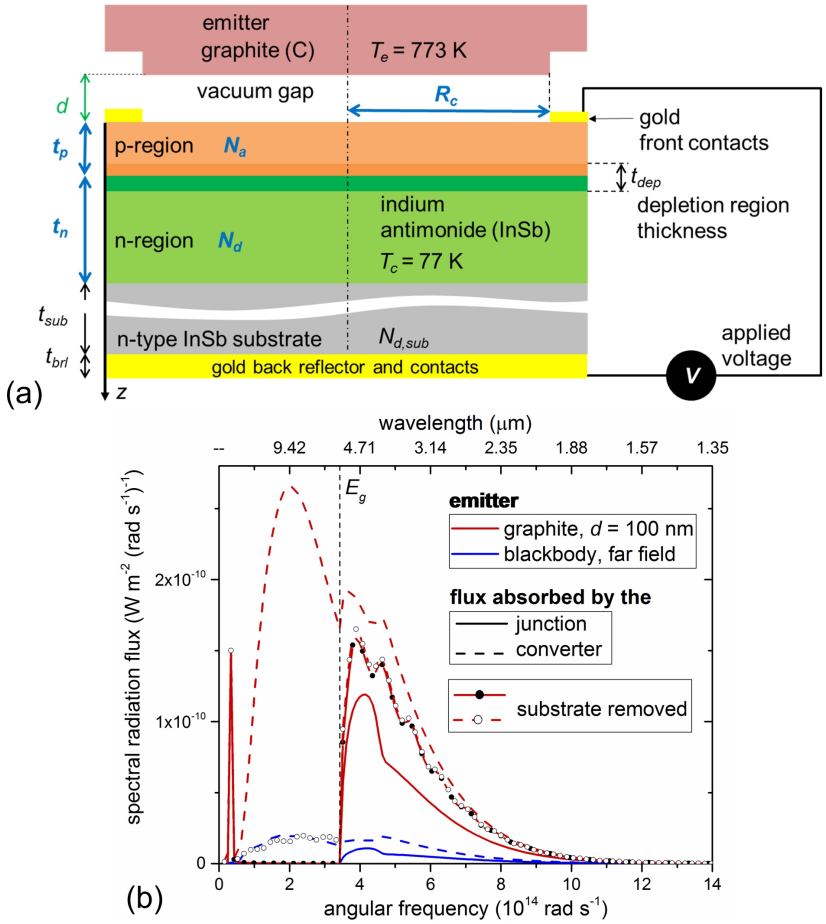

Fig. 1. (a) Schematic of the near-field thermophotovoltaic converter. The parameters to be determined for maximizing electrical power output are in blue bold font. (b) Spectral radiation flux absorbed by the p-n junction and the receiver, when the emitter is either made of graphite and the vacuum gap thickness is d = 100 nm, or a blackbody in the far field. The parameters of the p-n junction are those of case 2-1-1 described in section 3.2.

eV at 77 K), the conduction band is easily filled-in and the semiconductor becomes degenerate. As a consequence, an optical bandgap must be considered as explained by Burstein and Moss [50,51]. The transparency resulting from the so-called Moss-Burstein effect, experimentally observed in [52], can be accounted for by using the model for the absorption coefficient introduced in [66] and subsequently applied in [67] and more particularly in [68] for simulating InSb devices. Eqs. (14) with (2) and (16) with (17) and (18) from [66] are used with parameters (with proper units) provided in Table 2. The Fermi level E_f (noted F in [66]) is required. It is found by using an iterative dichotomy-based process that searches for the Fermi level matching the concentration of electrons in the conduction band (or holes in the valence band) as following [69]:

$$n = N\left[\mathcal{F}_{1/2}(\eta) + \frac{15\alpha kT}{4}\mathcal{F}_{3/2}(\eta) + \frac{105(\alpha kT)^2}{32}\mathcal{F}_{5/2}(\eta)\right] \quad (1)$$

where in a n-doped layer $n = N_d$ (doping concentration), $N = N_c$ (effective density of states in the conduction band), $\eta = (E_f - E_c)/kT$ (reduced Fermi level, with $E_c = E_g(T)$) [69], in a

p-doped layer $n = N_a$ (doping concentration), $N = N_v$ (effective density of states in the valence band), $\eta = -E_f/kT$ [63], and $\mathcal{F}_j$ is the Fermi-Dirac integral of order j [70]. Simple first-order asymptotic developments of these integrals for orders 1/2, 3/2 et 5/2 are available [70]. However, comparisons against exact data [71] show that they are not accurate for moderate to low reduced Fermi levels. Instead, series expansions from [72] are used for orders 1/2 and 3/2, and the more computing-time-consuming one from [73, 74] is applied for order 5/2. Calculations provide the interband absorption coefficient (κ), and thus the extinction coefficient ($k = (c_0\kappa)/(2\omega)$) of the complex refractive index ($m = n + ik$), for photon energies above the bandgap. The missing real part of the complex refractive index is determined using the Kramers-Krönig relation [75] and the complex permittivity calculated for photon energies below the bandgap, as detailed hereafter.

Table 2. Parameters for calculating the interband absorption coefficient of InSb using the model described in [66].

non-parabolicity factor α (eV^{-1})	$1/E_g$ [67]
matrix element of momentum operator P (eV cm)	$8.7\,10^{-8}$ [76]
Planck constant $\hbar$ (eV s)	6.582121
m_0 (eV/(c_0^2)) with c_0 in cm/s	$0.51099906\,10^6$
Boltzmann constant k (eV K^{-1})	$8.617385\,10^{-5}$
high frequency permittivity ε_∞	15.68 [77]

For photon energies smaller than the bandgap, optical properties are governed by the free-carriers and phonons. The Drude-Lorentz formulation of the complex permittivity is an appropriate model [78]:

$$\varepsilon(\omega) = \varepsilon_\infty \left(1 + \frac{\omega_{LO}^2 - \omega_{TO}^2}{\omega_{TO}^2 - \omega^2 - i\omega\gamma} - \frac{\omega_p^2}{\omega(\omega + i\Gamma)}\right) \tag{2}$$

where the high frequency permittivity $\varepsilon_\infty = 15.68$ at 100 K [77], $\omega_{TO} = 180$ cm^{-1}, $\omega_{L0} = 190.3$ cm^{-1} and $\gamma = 3.2$ cm^{-1} at 100 K [78]. The plasma frequency and damping coefficient for the Drude model are defined as:

$$\omega_p^2 = \frac{Ne^2}{\varepsilon_0\varepsilon_\infty m^*} \tag{3}$$

$$\Gamma = \frac{Ne^2\rho}{m^*} \tag{4}$$

where e is the elementary charge ($1.60217733\,10^{-19}$ C), ε_0 is the permittivity of vacuum ($8.854187817\,10^{-12}$ F m^{-1}), N is the doping concentration in the layer, m^* is the effective mass of the carrier under consideration, and ρ is the electrical resistivity (Ω cm). For example, electrons in a n-doped layer are majority carriers with $m^* = m_e^*$ (see Table 1), $N = N_d$ and $\rho = \rho_e(N_d, T)$. Similarly holes in a p-doped layer are majority carriers with $m^* = m_{dh}^*$, $N = N_a$ and $\rho = \rho_h(N_a, T)$. For a minority carrier, the proper doping concentration must be picked (e.g. N_a for electrons in a p-doped layer).
Electrical resistivity of electrons and holes is linked to mobility ($\rho(N,T) = (eN\mu(N,T))^{-1}$), expressed by a Caughey-Thomas model [79]:

Optics EXPRESS

$$\mu(N,T) = \mu_{\min} + \frac{\mu_{\max}\,(300/T)^{\theta_1} - \mu_{\min}}{1 + \left(\frac{N}{N_{\mathrm{ref}}(T/300)^{\theta_2}}\right)^{\phi}} \tag{5}$$

with parameters for InSb taken from [80], where parameters θ_1 and θ_2 are missing. Those are inferred from a non-linear fitting of conductivity ($1/\rho$) data available in [81] (see Table 3).

Table 3. Parameters of the Caughey-Thomas model for the mobility of electrons and holes in InSb.

	electrons	holes	
N (cm^{-3})	doping concentration in the layer		
$\mu_{\max}$ (cm^{-2} V^{-1} s^{-1})	78,000	750	
$\mu_{\min}$ (cm^{-2} V^{-1} s^{-1})	5,000	100	[80]
N_{ref} (cm^{-3})	$7\,10^{16}$	$6\,10^{17}$	
ϕ	0.7	0.6	
θ_1	0.91	1.85	this work
θ_2	0.07	2.9	

The other parameters for making the electrical simulations are taken from [54]: Shockley-Read-Hall radiative lifetimes of electrons and holes ($\tau_{SRH,e} = 10^{-10}$ s, $\tau_{SRH,h} = 10^{-6}$ s), Auger and radiative recombination parameters ($C = 5\,10^{-26}$ cm^6 s and $B = 5\,10^{-11}$ cm^6 s), and surface recombination velocities of electrons and holes ($S_e = 5\,10^4$ m s^{-1}, $S_h = 500$ m s^{-1}).

2.3. Radiation and electrical modeling

With the optical and electrical properties defined in the previous section, simulations of 1D Cartesian steady-state radiation transfer from the emitter to the cell and electrical transport in the InSb p-n junction are performed with models described elsewhere (see the methods section in [27] for a summary, and [10, 15] for more details). In summary, the spatial distribution of radiation power density absorbed in the layers of the junction is calculated using fluctuational electrodynamics and the S-matrix method for layered media [82]. The main difference with previous works is a larger number of layers (emitter, vacuum gap, p-doped layer, n-doped layer, n-doped substrate layer, back reflector layer and vacuum). Calculations are made over the spectral interval [$1.5193\,10^{13}$, $1.8837\,10^{15}$] rad s^{-1} ([0.01, 1.24] eV, [1.0, 123.98] μm) which covers more than 99% of the blackbody radiation power at the temperature of the emitter (T_e = 773 K). Under the assumption of low injection of photogenerated carriers, the minority carrier diffusion equations are solved with and without illumination to give the photocurrent and diode dark current densities, and then the current density - voltage characteristics $j(V)$. The series resistance ($R_{s,sub}$) due to transverse flow of electrons in the substrate and ($R_{s,lat}$) due to the lateral flow of holes in the p-doped layer to reach the contacts, must be accounted for. For a radius R_c of the active area of the cell, the $I(V')$ characteristic that includes these additional resistances is such that:

Optics EXPRESS

$$I(V') = I(V) = j(V)A_c \tag{6}$$

$$V' = V - (R_{s,sub} + R_{s,lat})\, I(V) \tag{7}$$

$$R_{s,sub} = \rho_e(N_{d,sub}, T)\, t_{sub}/A_c \tag{8}$$

$$R_{s,lat} = \frac{1}{8\pi}\rho_h(N_a, T)/t_p \tag{9}$$

with $A_c = \pi R_c^2$ and where $\rho_e(N_{d,sub}, T)$ and $\rho_h(N_a, T)$ are the electrical resistivities of electrons in the substrate and of holes in the p-doped layer, and expression of the sheet resistance for a circular contact is taken from [83].

It is important to note that efficiency of the NF-TPV converter is the ratio of electrical power at the maximum power point to radiation power absorbed by the whole receiver (p-n junction, substrate and back reflector). These three quantities (absorbed radiation power, electrical power, and efficiency) are functions of the vacuum gap distance (d) separating the emitter from the cell.

3. Results and discussion

In this section, results are presented for the operating conditions of the NF-TPV converter introduced in section 2.1 and Fig. 1. The only variable parameters are the thickness (t_p and t_n, with $t_p + t_n = 3$ μm) and doping concentration ($N_a \in [5\,10^{15}, 10^{17}]$ cm^{-3} and $N_d \in [3\,10^{14}, 4\,10^{17}]$ cm^{-3}) of the p- and n-layers of the junction, the radius (R_c) of the active part of the cell, and the vacuum gap thickness ($d \in [10$ nm, 10 μm$]$), within practical limits of fabrication and operation ranges.

3.1. Properties

When compared against experimental data [84], orders of magnitude of calculated mobilities are excellent for holes and fairly good for electrons. This is quite acceptable since the measurements were made with the Hall technique and thus should be corrected by the Hall factor [54]. In addition, mobility depends on the type of dopant and other carriers, and thus on if the carriers considered are majority or minority ones [85]. With this in mind, Fig. 2(a) shows a comparison of the calculated absorption coefficient with experimental data at 130 K [54], for various negative doping concentrations. The Moss-Burstein shift towards larger photon energies (smaller wavelengths) of the interband absorption edge with increasing electron concentration and free-carrier absorption levels are convincingly well predicted.

In Fig. 2(b), the absorption coefficient of n-doped InSb at 77 K is depicted as a function of the doping concentration. The clearly visible phonon polariton peak is likely to lower conversion performances because of sub-bandgap absorption [17]. Increasing the doping concentration has a double negative impact: it comes with a larger sub-bandgap absorption and a smaller interband absorption due to the Moss-Burstein effects. It is worth having in mind that at 300 K, this optical gap effect would be even larger, since the bandgap is smaller (0.17 eV). How these properties govern the optimum thickness and doping concentration of the p- and n-doped layers is analyzed next.

3.2. Optimum thickness and doping concentration of the p- and n-doped layers

By varying the doping concentration and thickness of the p-n junction layers as indicated in Table 4), 18 cases are investigated. They are named by a set of three natural numbers ($i - j - k$), respectively standing for the line number (1 to 3) for parameters N_a, N_d and the couple (t_p, t_n). After varying the vacuum gap distance d, a first result is that a hierarchy is established as a function of the various cases, for the curves of electrical power density at the maximum power point of the $j(V)$ characteristics (p_{max}, in W m^{-2}). In other words, the parameters maximizing

Optics EXPRESS

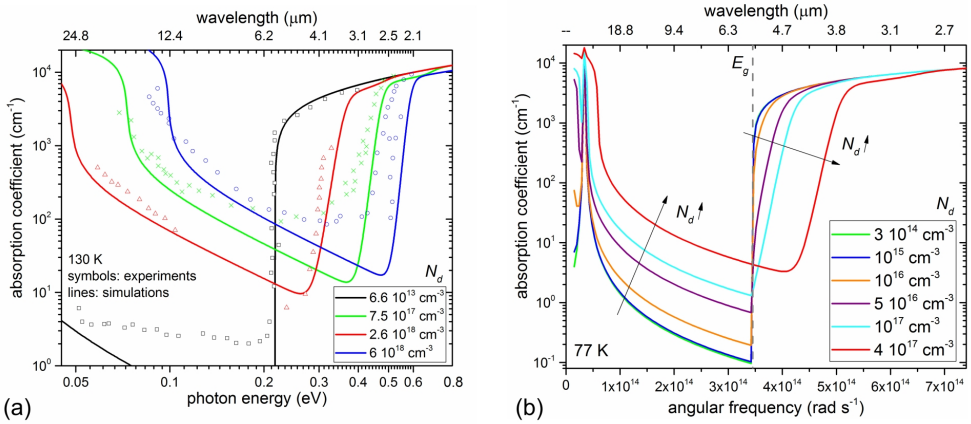

Fig. 2. Absorption coefficient of n-doped InSb as a function of doping concentration N_d: (a) at 130 K, comparison of simulations with experimental data in [54]. (b) at 77 K, impact on interband and free carrier absorption.

the power output of the cell do not depend on distance between the emitter and the cell (this is not the case for conversion efficiency, and this may not be the case with an emitter supporting phonon polaritons [27]). As a consequence, the plots of Fig. 3 are made for a single vacuum gap thickness (d=100 nm).

Table 4. Selected values for the variable parameters (18 different cases).

case	i	j	k
i, j, k values ↓	N_a (cm^{-3})	N_d (cm^{-3})	t_p, t_n (μm)
1	10^{16}	10^{15}	0.5, 2.5
2	10^{17}	$5\,10^{16}$	1.5, 1.5
3		10^{17}	2.5, 0.5

In Fig. 3(a) the electrical power density at the maximum power point is shown in increasing order for selected cases. The radiation flux density absorbed through the interband process, i.e. generating electron-hole pairs (EHP), is superimposed. Globally, the electrical power output follows the trend of sup-bandgap radiation absorption. By comparing cases 2-3-1, 2-2-1 and 2-1-1, where only the n-doping concentration (N_d) is changed, the Moss-Burstein effect can be observed (see the corresponding absorption coefficient spectra on Fig. 2(b)). When the n-doping concentration is the largest (10^{17} cm^{-3}, $j = 3$), there is less interband absorption, and thus optical losses. This is confirmed on the left part of Fig. 3(c), where spectral and spatial distributions of radiation flux density absorbed in discrete layers (of thickness $\Delta z = 6.25$ nm) of the p-n junction are plotted in case 2-3-1. Conversely, the right part of the same figure (case 2-1-1) indicates that a low n-doping concentration (10^{15} cm^{-3}, $j = 1$) has to be selected to avoid the optical gap shift. This selection is applied in the last four cases depicted in Figs. 3(a) and (b). Only the p-doping concentration (N_a) and the thicknesses of the p- and n- layers (t_p and t_n) are changed. Position and thickness of the depletion layer, and the built-in voltage, are impacted

Optics EXPRESS

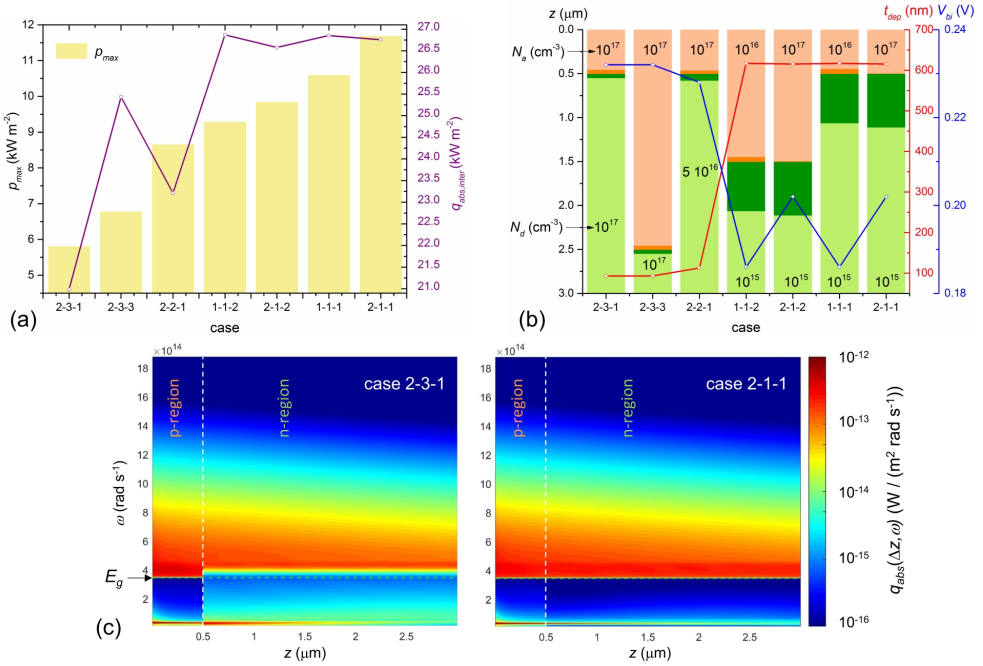

Fig. 3. For a vacuum gap thickness d = 100 nm and selected cases in Table 4: (a) electrical power density at the maximum power point (p_{max}) and radiation flux density absorbed through the interband process - generating electron-hole pairs - ($q_{abs,inter}$). (b) p-doped, depletion and n-doped layers of the active part of the cell, depletion layer thickness (t_{dep}), and built-in voltage (V_{bi}). (c) Spectral and spatial distributions of radiation flux density absorbed in discrete layers (Δz = 6.25 nm) within the active part of the cell, in cases 2-3-1 and 2-1-1.

by these changes, as indicated in Fig. 3(b). About the depletion layer, its thickness is almost similar in these cases, thus only its position matters. When the thickness of the p-layer is the largest (k = 3), the depletion layer is too far from the front of the cell, where absorption is the largest. Thus it is preferable to have a p-layer thickness of 0.5 μm. Finally, it is with the largest p-doping concentration (10^{17} cm^{-3}, i = 2) that the potential barrier (V_{bi}) is the largest, allowing the cell to perform better. Additional calculations show that: (i) a thinner p-doped layer does not improve substantially the power output of the cell; (ii) when the emitter temperature is increased, the optical gap effect still leads to optical losses, which decrease without being negligible (e.g. when T_e= 1273 K and d= 100 nm, the electrical power density at the maximum power point is still enhanced by a factor 1.74 from the worst case 2-1-1 with N_d = 10^{17} cm^{-3} to the best case 2-3-1 with N_d = 10^{15} cm^{-3}). Then within the limits of fabrication constraints, the parameters maximizing electrical power output are N_a = 10^{17} cm^{-3} with t_p=0.5 μm, and N_d = 10^{15} cm^{-3} with t_n=2.5 μm. It is worth mentioning that the same parameters maximize efficiency.

3.3. *Impact of sub-bandgap absorption and series resistance losses*

With the optimum parameters found in the previous section, impact of sub-bandgap absorption and series resistance losses on conversion efficiency is assessed. Under high illumination, series resistance losses become an issue, since the corresponding power loss scales as the square of the current. For example, it is common to have spacing of 200 μm or less between contact fingers in solar concentrated photovoltaic cells with a concentration factor of 1000 [86]. In

Optics EXPRESS

thermophotovoltaic devices, illumination levels are comparable, in particular when the distance between the emitter and the cell is a few hundreds of nanometers or less.

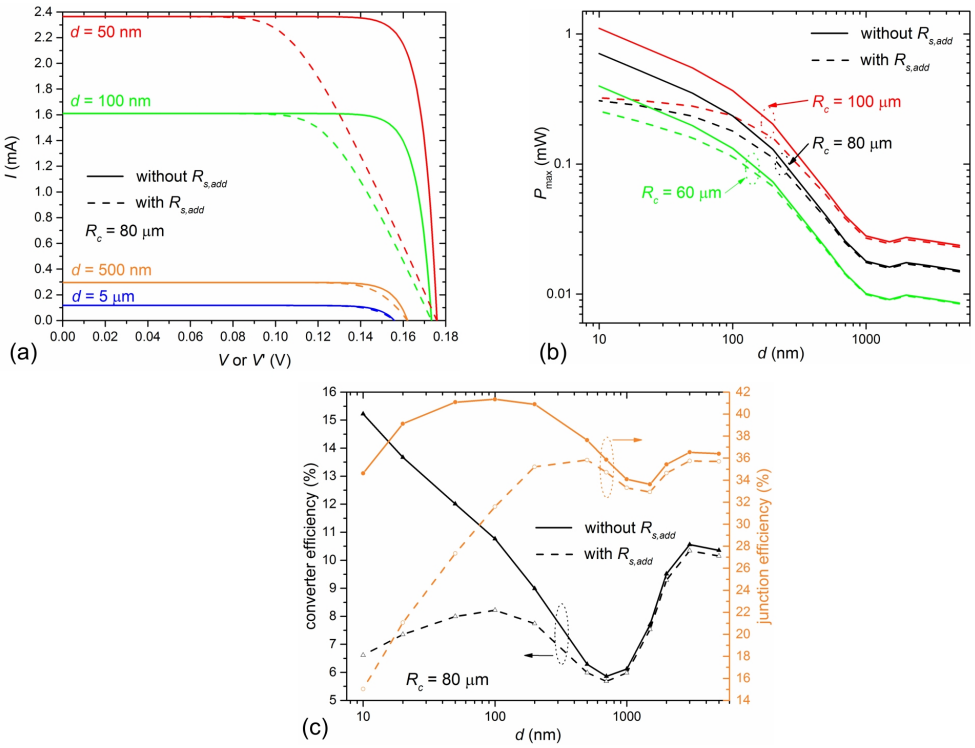

Fig. 4. Impact of the additional series resistance ($R_{s,add}$) on: (a) current-voltage characteristics when the radius of the active part of the cell is R_c = 80 μm, (b) electrical power at the maximum power point for three values of R_c, and (c) junction and converter efficiencies when R_c = 80 μm, as a function of the vacuum gap thickness.

Thus in order to avoid too large series resistance losses, the radius of the active part of the cell (R_c) must be of the order of dozens of micrometers. Figure 4 shows that series resistance losses are seriously detrimental to the performances of the converter for vacuum gap thicknesses smaller than 500 nm. Current-voltage characteristics without and with including the additional series resistances ($R_{s,add} = R_{s,sub} + R_{s,lat}$, see section 2.3) depicted in Fig. 4(a) highlight unambiguously this effect when R_c = 80 μm. Electrical power output and conversion efficiency of the junction only and of the converter (absorption by the substrate and back contacts is added) are plotted as a function of vacuum gap thickness in Figs. 4(b) and (c), respectively. For the electrical power, at the largest vacuum gap thicknesses, a local maximum and a local minimum are visible. These specific variations are resulting from the interference effects taking place in the coherent regime of thermal radiation between parallel media [87, 88]. Below the vacuum gap thickness where there is a local minimum, electrical power increases because of the contribution of evanescent waves, as expected. Three values of the radius of the active area of the cell (R_c = 60, 80 and 100 μm) are considered. If series resistance losses are omitted, it makes sense to have the cell with the largest area. However, when ohmic losses are added, the near-field enhancement of electrical power is lowered. Since these losses depend on the square of the current, they grow with the active area and when the vacuum gap distance is decreased. As a result, for d = 10 nm, the cell with R_c = 100 μm does not perform any better than that with R_c = 80 μm. It must be emphasized that these series resistance losses will increase for larger emitter temperatures. As

for efficiency, its variations with vacuum gap thickness are governed by the relative variations of electrical power and absorbed radiation power. In addition to the series resistance losses, sub-bandgap absorption has a tremendous impact on efficiency. The decline of the junction efficiency when the vacuum gap thickness is smaller than 100 nm is caused by a huge increase of radiation transfer involving the phonon polariton of InSb (see Fig. 1(b)). This is a known issue for III-V materials [17] which can be solved only by preventing the emitter to be active in the corresponding spectral range. With the present emitter and cell temperatures (773 K and 77 K), the maximum (Carnot) efficiency is 90 %. If the junction efficiency is quite substantial (32 % or more), it is maximum (36 %) for a vacuum gap thickness of 500 nm. Below that value, efficiency drops because of the series resistance losses. The converter efficiency is much smaller (at least 19 % less) because of sub-bandgap radiation absorption by free carriers in the substrate (see Fig. 1(b)), caused by the large doping concentration (see Fig. 2(b)). The combination of sub-bandgap absorption and series resistance losses leads to a maximum efficiency in the near field of 8.2 % at a vacuum gap thickness of 100 nm. In order to avoid this, lowering the doping concentration must be considered with care because of the additional series resistance. The best option would be to remove the substrate [89] after the MBE growth of the p-n junction layers and before processing the contacts, while ensuring the cell mechanical sustainability. If it were possible to do so, calculations show that for a vacuum gap thickness of 100 nm, the electrical power density would be enhanced by a factor 1.5, and the efficiency of the converter by a factor 3 (24.9 %) in the case with R_c=80 μm, thanks to a huge reduction in sub-bandgap absorption (see Fig. 1(b)).

4. Conclusion

In this article, it has been shown that appropriate optical and electrical properties and realistic fabrication and operating conditions must be accounted for when designing the photovoltaic cell in a NF-TPV converter. In the specific case of a photovoltaic cell made of indium antimonide, a p-n junction cannot be functional at 300K and must be cooled down to much lower temperatures. The bandgap of InSb being small, n-doped InSb is easily degenerate at large doping concentrations. It has been shown that the resulting optical gap effect must be properly taken into account in the calculation of absorption for photon energies larger than the bandgap. Within acceptable ranges, optimum doping concentration and thickness of the p-n junction layers have been determined. It has been revealed that because of high currents, the lateral series resistance losses have huge detrimental impacts on the performances of the NF-TPV converter, unless micro-cells are used or other strategies are applied [30]. Finally, the issue of sub-bandgap phonon polariton and free carrier absorption remains to be solved for avoiding deterioration of the converter efficiency. Even though the NF-TPV converter based on an InSb photovoltaic cell described in the present article is meant to be for a laboratory experiment, and not for a practical device because of the cooling constraint, it is believed that the same methods can be used for designing the photovoltaic cell in NF-TPV devices based on other low bandgap III-V materials.

Funding

French National Research Agency (ANR) (ANR-16-CE05-0013). Partial funding by the French "Investment for the Future" program (EquipEx EXTRA, ANR-11-EQPX-0016) and by the Occitanie region.

Acknowledgments

R.V. is thankful to the Department of Mechanical Engineering at the University of Utah (U of U) for hosting him in 2016 and 2017, to the Instituto de Energía Solar at the Universidad Politécnica de Madrid (UPM) for hosting him in 2018, and to D. Milovich, M. Francoeur, J. DeSutter (U of

Optics EXPRESS

U), A. Datas, E. Antolin, J. Villa, and A. Marti (UPM) for fruitful discussions. The authors are thankful to the anonymous reviewers for their constructive remarks and suggestions.

References

1. J. L. Pan, H. K. Choy, and C. Fonstad, "Very large radiative transfer over small distances from a black body for thermophotovoltaic applications," IEEE Transactions on Electron Devices **47**, 241–249 (2000).
2. M. Whale and E. G. Cravalho, "Modeling and performance of microscale thermophotovoltaic energy conversion devices," IEEE Transactions on Energy Convers. **17**, 130–142 (2002).
3. A. Narayanaswamy and G. Chen, "Surface modes for near field thermophotovoltaics," Appl. Phys. Lett. **82**, 3544–3546 (2003).
4. M. Laroche, R. Carminati, and J.-J. Greffet, "Near-field thermophotovoltaic energy conversion," J. Appl. Phys. **100**, 063704 (2006).
5. O. Ilic, M. Jablan, J. D. Joannopoulos, I. Celanovic, and M. Soljačić, "Overcoming the black body limit in plasmonic and graphene near-field thermophotovoltaic systems," Opt. Express **20**, A366–A384 (2012).
6. S. Basu, Y.-B. Chen, and Z. Zhang, "Microscale radiation in thermophotovoltaic devices – a review," Int. J. Energy Res. **31**, 689–716 (2007).
7. K. Park, S. Basu, W. King, and Z. Zhang, "Performance analysis of near-field thermophotovoltaic devices considering absorption distribution," J. Quant. Spectrosc. Radiat. Transf. **109**, 305–316 (2008).
8. S. Basu, Z. Zhang, and C. Fu, "Review of near-field thermal radiation and its application to energy conversion," Int. J. Energy Res. **33**, 1203–1232 (2009).
9. X. Zhai, J. Lai, H. Liang, and S. Chen, "Performance analysis of thermophotovoltaic system with an equivalent cut-off blackbody emitter," J. Appl. Phys. **108**, 074507 (2010).
10. M. Francoeur, R. Vaillon, and M. P. Mengüç, "Thermal impacts on the performance of nanoscale-gap thermophotovoltaic power generators," IEEE Transactions on Energy Convers. **26**, 686–698 (2011).
11. R. Messina and P. Ben-Abdallah, "Graphene-based photovoltaic cells for near-field thermal energy conversion," Sci. Reports **3**, 1383 (2013).
12. T. Bright, L. Wang, and Z. Zhang, "Performance of near-field thermophotovoltaic cells enhanced with a backside reflector," J. Heat Transf. **136**, 062701 (2014).
13. I. Latella, A. Pérez-Madrid, L. C. Lapas, and J. Miguel Rubi, "Near-field thermodynamics: Useful work, efficiency, and energy harvesting," J. Appl. Phys. **115**, 124307 (2014).
14. V. Svetovoy and G. Palasantzas, "Graphene-on-silicon near-field thermophotovoltaic cell," Phys. Rev. Appl. **2**, 034006 (2014).
15. M. P. Bernardi, O. Dupré, E. Blandre, P.-O. Chapuis, R. Vaillon, and M. Francoeur, "Impacts of propagating, frustrated and surface modes on radiative, electrical and thermal losses in nanoscale-gap thermophotovoltaic power generators," Sci. Reports **5**, 11626 (2015).
16. J.-Y. Chang, Y. Yang, and L. Wang, "Tungsten nanowire based hyperbolic metamaterial emitters for near-field thermophotovoltaic applications," Int. J. Heat Mass Transf. **87**, 237–247 (2015).
17. K. Chen, P. Santhanam, and S. Fan, "Suppressing sub-bandgap phonon-polariton heat transfer in near-field thermophotovoltaic devices for waste heat recovery," Appl. Phys. Lett. **107**, 091106 (2015).
18. A. Karalis and J. Joannopoulos, "Temporal coupled-mode theory model for resonant near-field thermophotovoltaics," Appl. Phys. Lett. **107**, 141108 (2015).
19. I. Latella, A. Pérez-Madrid, L. C. Lapas, and J. M. Rubi, "Near-field thermodynamics and nanoscale energy harvesting," Phys. Scripta **2015**, 014026 (2015).
20. M. Lim, S. Jin, S. S. Lee, and B. J. Lee, "Graphene-assisted si-InSb thermophotovoltaic system for low temperature applications," Opt. Express **23**, A240–A253 (2015).
21. S. Molesky and Z. Jacob, "Ideal near-field thermophotovoltaic cells," Phys. Rev. B **91**, 205435 (2015).
22. J. K. Tong, W.-C. Hsu, Y. Huang, S. V. Boriskina, and G. Chen, "Thin-film thermal well emitters and absorbers for high-efficiency thermophotovoltaics," Sci. reports **5**, 10661 (2015).
23. S. Jin, M. Lim, S. S. Lee, and B. J. Lee, "Hyperbolic metamaterial-based near-field thermophotovoltaic system for hundreds of nanometer vacuum gap," Opt. express **24**, A635–A649 (2016).
24. A. Karalis and J. Joannopoulos, "Squeezing near-field thermal emission for ultra-efficient high-power thermophotovoltaic conversion," Sci. Reports **6**, 28472 (2016).
25. J. Z.-J. Lau, V. N.-S. Bong, and B. T. Wong, "Parametric investigation of nano-gap thermophotovoltaic energy conversion," J. Quant. Spectrosc. Radiat. Transf. **171**, 39–49 (2016).
26. M. Mirmoosa, M. Omelyanovich, and C. Simovski, "Microgap thermophotovoltaic systems with low emission temperature and high electric output," J. Opt. **18**, 115104 (2016).
27. E. Blandre, P.-O. Chapuis, and R. Vaillon, "High-injection effects in near-field thermophotovoltaic devices," Sci. Reports **7**, 15860 (2017).
28. J. DeSutter, R. Vaillon, and M. Francoeur, "External luminescence and photon recycling in near-field thermophotovoltaics," Phys. Rev. Appl. **8**, 014030 (2017).
29. M. Elzouka and S. Ndao, "Towards a near-field concentrated solar thermophotovoltaic microsystem: Part i–modeling," Sol. Energy **141**, 323–333 (2017).

Optics EXPRESS

30. A. Karalis and J. Joannopoulos, "Transparent and opaque conducting electrodes for ultra-thin highly-efficient near-field thermophotovoltaic cells," Sci. Reports **7**, 14046 (2017).
31. J. Z.-J. Lau and B. T. Wong, "Thermal energy conversion using near-field thermophotovoltaic device composed of a thin-film tungsten radiator and a thin-film silicon cell," J. Appl. Phys. **122**, 084302 (2017).
32. T. Liao, Z. Yang, W. Peng, X. Chen, and J. Chen, "Parametric characteristics and optimum criteria of a near-field solar thermophotovoltaic system at the maximum efficiency," Energy Convers. Manag. **152**, 214–220 (2017).
33. T. Liao, Z. Yang, Q. Dong, X. Chen, and J. Chen, "Performance evaluation and parametric optimum choice criteria of a near-field thermophotovoltaic cell," IEEE Transactions on Electron Devices **64**, 4144–4148 (2017).
34. M. Lim, S. S. Lee, and B. J. Lee, "Effects of multilayered graphene on the performance of near-field thermophotovoltaic system at longer vacuum gap distances," J. Quant. Spectrosc. Radiat. Transf. **197**, 84–94 (2017).
35. M. Mirmoosa, S.-A. Biehs, and C. Simovski, "Super-planckian thermophotovoltaics without vacuum gaps," Phys. Rev. Appl. **8**, 054020 (2017).
36. R. St-Gelais, G. R. Bhatt, L. Zhu, S. Fan, and M. Lipson, "Hot carrier-based near-field thermophotovoltaic energy conversion," ACS nano **11**, 3001–3009 (2017).
37. N. Vongsoasup, M. Francoeur, and K. Hanamura, "Performance analysis of near-field thermophotovoltaic system with 2d grating tungsten radiator," Int. J. Heat Mass Transf. **115**, 326–332 (2017).
38. B. Wang, C. Lin, and K. H. Teo, "Near-field thermophotovoltaic system design and calculation based on coupled-mode analysis," J. Photonics for Energy **7**, 044501 (2017).
39. J. Watjen, X. Liu, B. Zhao, and Z. Zhang, "A computational simulation of using tungsten gratings in near-field thermophotovoltaic devices," J. Heat Transf. **139**, 052704 (2017).
40. Y. Yang, J.-Y. Chang, P. Sabbaghi, and L. Wang, "Performance analysis of a near-field thermophotovoltaic device with a metallodielectric selective emitter and electrical contacts for the photovoltaic cell," J. Heat Transf. **139**, 052701 (2017).
41. H. Yu, D. Liu, Z. Yang, and Y. Duan, "Simple rectangular gratings as a near-field anti-reflection pattern for GaSb tpv cells," Sci. Reports **7**, 1026 (2017).
42. B. Zhao, K. Chen, S. Buddhiraju, G. Bhatt, M. Lipson, and S. Fan, "High-performance near-field thermophotovoltaics for waste heat recovery," Nano Energy **41**, 344–350 (2017).
43. T. Inoue, K. Watanabe, T. Asano, and S. Noda, "Near-field thermophotovoltaic energy conversion using an intermediate transparent substrate," Opt. Express **26**, A192–A208 (2018).
44. M. Lim, J. Song, J. Kim, S. S. Lee, I. Lee, and B. J. Lee, "Optimization of a near-field thermophotovoltaic system operating at low temperature and large vacuum gap," J. Quant. Spectrosc. Radiat. Transf. **210**, 35–43 (2018).
45. E. Tervo, E. Bagherisereshki, and Z. Zhang, "Near-field radiative thermoelectric energy converters: a review," Front. Energy **12**, 5–21 (2018).
46. H. Yu, Y. Duan, and Z. Yang, "Selectively enhanced near-field radiative transfer between plasmonic emitter and GaSb with nanohole and nanowire periodic arrays for thermophotovoltaics," Int. J. Heat Mass Transf. **123**, 67–74 (2018).
47. H. Yu, D. Liu, Y. Duan, and Z. Yang, "Four-layer metallodielectric emitter for spectrally selective near-field radiative transfer in nano-gap thermophotovoltaics," J. Quant. Spectrosc. Radiat. Transf. **217**, 235–242 (2018).
48. A. Fiorino, L. Zhu, D. Thompson, R. Mittapally, P. Reddy, and E. Meyhofer, "Nanogap near-field thermophotovoltaics," Nat. Nanotechnol. **13**, 608–811 (2018).
49. R. S. DiMatteo, P. Greiff, S. L. Finberg, K. A. Young-Waithe, H. Choy, M. M. Masaki, and C. G. Fonstad, "Enhanced photogeneration of carriers in a semiconductor via coupling across a nonisothermal nanoscale vacuum gap," Appl. Phys. Lett. **79**, 1894–1896 (2001).
50. E. Burstein, "Anomalous optical absorption limit in InSb," Phys. Rev. **93**, 632 (1954).
51. T. Moss, "The interpretation of the properties of indium antimonide," Proc. Phys. Soc. Sect. B **67**, 775 (1954).
52. G. Gobeli and H. Fan, "Infrared absorption and valence band in indium antimonide," Phys. Rev. **119**, 613 (1960).
53. J.-P. Mulet, K. Joulain, R. Carminati, and J.-J. Greffet, "Enhanced radiative heat transfer at nanometric distances," Microscale Thermophys. Eng. **6**, 209–222 (2002).
54. M. Levinshtein, M. Rumyantsev, and M. Shur, *Handbook Series On Semiconductor Parameters, Vol. 1: Si, Ge, C (Diamond), GaAs, GaP, GaSb, InAs, InP, InSb*, vol. 1 (World Scientific, 1996).
55. F. Hopkins and J. Boyd, "Dark current analysis of InSb photodiodes," Infrared Phys. **24**, 391–395 (1984).
56. I. Kanno, F. Yoshihara, R. Nouchi, O. Sugiura, Y. Murase, T. Nakamura, and M. Katagiri, "Radiation measurements by a cryogenic pn junction InSb detector with operating temperatures up to 115 k," Rev. Sci. Instruments **74**, 3968–3973 (2003).
57. J. Abautret, J. Perez, A. Evirgen, F. Martinez, P. Christol, J. Fleury, H. Sik, R. Cluzel, A. Ferron, and J. Rothman, "Electrical modeling of InSb pin photodiode for avalanche operation," J. Appl. Phys. **113**, 183716 (2013).
58. S. Maimon and G. Wicks, "n b n detector, an infrared detector with reduced dark current and higher operating temperature," Appl. Phys. Lett. **89**, 151109 (2006).
59. E. G. Camargo, K. Ueno, T. Morishita, H. Goto, N. Kuze, K. Sawada, and M. Ishida, "Performance improvement of molecular beam epitaxy grown InSb photodiodes for room temperature operation," Jpn. J. Appl. Phys. **47**, 8430 (2008).
60. N. Kuze, T. Morishita, E. Camargo, K. Ueno, A. Yokoyama, M. Sato, H. Endo, Y. Yanagita, S. Tokuo, and H. Goto, "Development of uncooled miniaturized InSb photovoltaic infrared sensors for temperature measurements," J. Cryst. Growth **311**, 1889–1892 (2009).

Optics EXPRESS

61. A. Evirgen, J. Abautret, J. Perez, A. Cordat, A. Nedelcu, and P. Christol, "Midwave infrared InSb nbn photodetector," Electron. Lett. **50**, 1472–1473 (2014).
62. I. Vurgaftman, J. á. Meyer, and L. á. Ram-Mohan, "Band parameters for iii–v compound semiconductors and their alloys," J. Appl. Phys. **89**, 5815–5875 (2001).
63. S. M. Sze and K. K. Ng, *Physics of semiconductor devices* (John wiley & sons, 2006).
64. M. R. Querry, "Optical properties of graphite pellets (a)," J. Opt. Soc. Am. A **2** (1985).
65. I. Latella, P. Ben-Abdallah, S.-A. Biehs, M. Antezza, and R. Messina, "Radiative heat transfer and nonequilibrium casimir-lifshitz force in many-body systems with planar geometry," Phys. Rev. B **95**, 205404 (2017).
66. W. Anderson, "Absorption constant of pb1-xsnxte and hg1-xcdxte alloys," Infrared Phys. **20**, 363–372 (1980).
67. J. Chu and A. Sher, *Physics and properties of narrow gap semiconductors* (Springer, 2008).
68. Z. Djuric, B. Livada, V. Jovic, M. Smiljanic, M. Matic, and Z. Lazic, "Quantum efficiency and responsivity of InSb photodiodes utilizing the moss-burstein effect," Infrared Phys. **29**, 1–7 (1989).
69. E. Sijerčić, K. Mueller, and B. Pejčinović, "Simulation of InSb devices using drift–diffusion equations," Solid-State Electron. **49**, 1414–1421 (2005).
70. R. Kim and M. Lundstrom, "Notes on fermi-dirac integrals," arXiv preprint arXiv:0811.0116 (2008).
71. J. Blakemore, *Semiconductor Statistics. International Series of Monographs on Semiconductors, Vol. 3* (Pergamon Press: Oxford, 1962).
72. X. Aymerich-Humet, F. Serra-Mestres, and J. Millan, "An analytical approximation for the fermi-dirac integral f32 (η)," Solid-State Electron. **24**, 981–982 (1981).
73. P. Van Halen and D. Pulfrey, "Accurate, short series approximations to fermi–dirac integrals of order- 1/2, 1/2, 1, 3/2, 2, 5/2, 3, and 7/2," J. Appl. Phys. **57**, 5271–5274 (1985).
74. P. Van Halen and D. Pulfrey, "Erratum: Accurate, short series approximation to fermi–dirac integrals of order- 1/2, 1/2, 1, 3/2, 2, 5/2, 3, and 7/2 [j. appl. phys. 5 7, 5271 (1985)]," J. Appl. Phys. **59**, 2264–2265 (1986).
75. V. Lucarini, J. J. Saarinen, K.-E. Peiponen, and E. M. Vartiainen, *Kramers-Kronig relations in optical materials research*, vol. 110 (Springer Science & Business Media, 2005).
76. O. Madelung, *Physics of III-V compounds* (J. Wiley, 1964).
77. R. Sanderson, "Far infrared optical properties of indium antimonide," J. Phys. Chem. Solids **26**, 803–810 (1965).
78. R. Gammon and E. Palik, "Attenuated-total-reflection spectral linewidth: Analysis of surface-polariton dispersion relations and damping rates," JOSA **64**, 350–356 (1974).
79. D. Caughey and R. Thomas, "Carrier mobilities in silicon empirically related to doping and field," Proc. IEEE **55**, 2192–2193 (1967).
80. J. A. González-Cuevas, T. F. Refaat, M. N. Abedin, and H. E. Elsayed-Ali, "Modeling of the temperature-dependent spectral response of in 1–χ ga χ sb infrared photodetectors," Opt. Eng. **45**, 044001 (2006).
81. V. Orlov and G. Sergeev, "Numerical simulation of the transport properties of indium antimonide," Phys. Solid State **55**, 2215–2222 (2013).
82. M. Francoeur, M. P. Mengüç, and R. Vaillon, "Solution of near-field thermal radiation in one-dimensional layered media using dyadic green's functions and the scattering matrix method," J. Quant. Spectrosc. Radiat. Transf. **110**, 2002–2018 (2009).
83. N. C. Wyeth, "Sheet resistance component of series resistance in a solar cell as a function of grid geometry," Solid-State Electron. **20**, 629–634 (1977).
84. E. Litwin-Staszewska, W. Szymańska, and R. Piotrzkowski, "The electron mobility and thermoelectric power in InSb at atmospheric and hydrostatic pressures," Phys. Status Solidi (b) **106**, 551–559 (1981).
85. D. Martín and C. Algora, "Temperature-dependent GaSb material parameters for reliable thermophotovoltaic cell modelling," Semicond. Sci. Technol. **19**, 1040 (2004).
86. A. Luque and S. Hegedus, *Handbook of photovoltaic science and engineering* (John Wiley & Sons, 2003).
87. A. Narayanaswamy and J. Mayo, "Minimum radiative heat transfer between two metallic half-spaces due to propagating waves," J. Quant. Spectrosc. Radiat. Transf. **184**, 254–261 (2016).
88. Y. Tsurimaki, P.-O. Chapuis, J. Okajima, A. Komiya, S. Maruyama, and R. Vaillon, "Coherent regime and far-to-near-field transition for radiative heat transfer," J. Quant. Spectrosc. Radiat. Transf. **187**, 310–321 (2017).
89. T. Burger, D. Fan, K. Lee, S. R. Forrest, and A. Lenert, "Thin-film architectures with high spectral selectivity for thermophotovoltaic cells," ACS Photonics **5**, 2748–2754 (2018).